



OPEN

Modified unified critical state model for soils considering over-consolidation and cyclic loading behaviours

Xiaowen Wang¹, Ran Yuan² & Kai Cui³✉

This paper presents a modified unified critical state model to predict the mechanical responses of both clays and sands under over-consolidation and cyclic loading conditions on the basis of clay and sand model (CASM), which is named as CASM-kII. Through the application of subloading surface concept, CASM-kII is able to describe the plastic deformation inside the yield surface and the reverse plastic flow, and is thus expected to capture the over-consolidation and cyclic loading behaviours of soils. CASM-kII is numerically implemented by the use of the forward Euler scheme with automatic substepping and error control. Then, a sensitivity study is carried out to check the influences of the three new parameters of CASM-kII on the mechanical response of soils in over-consolidation and cyclic loading conditions. Through the comparisons of experimental data and simulated results, it is found that CASM-kII is able to satisfactorily describe the mechanical responses of both clays and sands in over-consolidation and cyclic loading conditions.

An accurate and concise description of the mechanical properties of soils is required for the design of civil engineering. As one of the most significant achievements in the field of geomechanics, Cam-clay plasticity¹ has been well accepted for the constitutive modeling of soils^{2–6}. In order to unify the constitutive modelling of both clays and sands, Yu⁷ developed a unified critical state model for clay and sand (i.e., CASM) on the basis of Cam-clay plasticity and state parameter concept. Owing to its concise mathematical expression and clear physical meaning of material constants, the CASM has been further developed to capture the more complex mechanical behaviours of soils^{8–12}.

However, as stated by Hashiguchi^{13–15}, classic elastoplastic constitutive models with a single yield surface enclosing the elastic domain possess many limitations in describing the mechanical response of soils. First, the original CASM predicts pure elastic behaviour inside the yield surface while the experimental data show that recoverable deformation only occurs within a very small range^{16–19}. CASM describes discontinuous variation of the tangent stiffness modulus from elastic to plastic of over-consolidated soils and predicts an unsmooth stress–strain relation, and thus is unable to describe softening behaviour accurately^{9,17,20}. Second, the ability to characterize the effect of stress history during cyclic loading process is significant to the constitutive modeling of soils^{21–25}, since it has been discovered in cyclic loading tests that elastic and plastic deformations both develop during unloading before the stress path is completely reversed^{26,27}. When the effect of reverse plastic flow is critical, the traditional isotropic hardening CASM model with a single yield surface is unable to provide appropriate solutions for boundary value problems because the reversed plastic flow fails to be considered just by expanding the single yield locus. Therefore, the above significant issues must be considered before further developing CASM to describe a variety of more complex properties of soils. Khong⁹ has attempted to introduce the concept of kinematic hardening into CASM within the context of bounding surface theory (i.e. CASM-k) but failed because of the difficulty of numerical implementation, thus Khong⁹ highly recommended that further development of CASM should be conducted in future research.

To extend the prediction ability of conventional elastoplastic constitutive model under complex loading conditions (such as over-consolidation, cyclic loading, anisotropic loading and non-proportional loading), Hashiguchi^{13–15} proposed the subloading surface concept with rigorous physical backgrounds. During last

¹School of Civil Engineering, Southwest Jiaotong University, Chengdu 610031, China. ²Key Laboratory of Transportation Tunnel Engineering, Ministry of Education, Southwest Jiaotong University, Chengdu 610031, China. ³Key Laboratory of High-Speed Railway Engineering, Ministry of Education, Southwest Jiaotong University, Chengdu 610031, China. ✉email: cuikai@swjtu.edu.cn

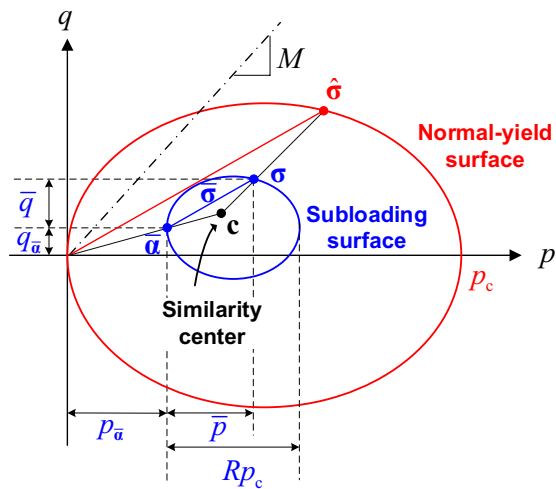


Figure 1. The relationship of subloading surface and normal-yield surface in p – q plane.

decades, subloading surface concept has been widely adopted in the constitutive modeling of soils. Hashiguchi et al.¹⁷ and Yao et al.¹⁸ adopted the subloading surface to describe the over-consolidated behaviour of soils. Asaoka et al.²⁸ and Zhang et al.²⁹ described the mechanical properties of structured soils through the combination of superloading and subloading surfaces. Since the concept of rotational hardening mechanism has been widely adopted in the constitutive modeling to capture the induced anisotropic properties of soils^{30–32}, Hashiguchi and Chen³³, Yamakawa et al.³⁴ and Hashiguchi et al.³⁵ combined the subloading surface concept with rotational hardening theory to characterize the cyclic mobility mechanism of anisotropic soils.

In this study, a new modified unified critical state model called CASM-kII is developed by introducing the subloading surface theory into the original CASM. This new model is established to extend the prediction ability of CASM for both clays and sands under over-consolidation and cyclic loading conditions. The plastic modulus of this new model is derived through the consistency condition of subloading function and varies smoothly from elastic to plastic response during loading procedure, which makes it possible for CASM-kII to characterize the plastic deformation inside the yield surface and the reverse plastic flow and thus to describe the over-consolidated behaviour and cyclic loading response of soils in a flexible fashion. Then, the forward Euler scheme with automatic substepping and error control is adopted in this study to numerical implement this newly proposed model. Compared with original CASM, CASM-kII adds three material parameters to control the evolution law of subloading surface, and the influences of these new parameters on the mechanical properties of soils under drained and undrained conditions is checked through a sensitivity study. At last, CASM-kII is validated through the comparisons of experimental data and simulation results in monotonic and cyclic loading tests under both drained and undrained conditions.

Constitutive relation of CASM-kII

First, soil behaviour is assumed to be isotropic in this paper for the sake of simplicity. If the inherent and induced anisotropy behaviours of soils need to be considered, CASM-kII may be extended to account for anisotropy by incorporating anisotropic mechanism such as rotational hardening behaviour^{30–35} or soil fabric and its evolution rule^{36–39} in the model. The extension work for the issue of anisotropy can be referred to the work of Gao et al.⁴⁰ Second, the bold-faced characters are used to represent vectors and tensors and the italics are used to represent scalars.

In this section, the subloading surface theory is introduced in CASM. The effective mean stress p and deviatoric stress q can be expressed as:

$$p = \frac{1}{3} \text{tr}(\boldsymbol{\sigma}), \quad q = \sqrt{\frac{3}{2}} \|\boldsymbol{\sigma} - p\boldsymbol{\delta}\| \quad (1)$$

where $\boldsymbol{\sigma}$ is effective stress tensor; $\boldsymbol{\delta}$ is Kronecker delta.

As illustrated in Fig. 1, it is assumed that a subloading surface exists inside the domain bounded by the typical yield surface (or called normal-yield surface), which indicates the loading history and represents the material's mechanical responses during the loading and unloading procedure^{13–15}. The subloading surface passes always through the current stress state $\boldsymbol{\sigma}$, and approaches the normal-yield surface asymptotically in a plastic loading procedure. During the whole loading process, the shapes of subloading surface and normal-yield surface keep similar, and the normal-yield ratio is recorded as R . According to the geometric relationships shown in Fig. 1, the following relationships can be given as:

$$\frac{\|\bar{\sigma}\|}{\|\hat{\sigma}\|} = \frac{\bar{p}}{\hat{p}} = \frac{\bar{q}}{\hat{q}} = \frac{Rp_c}{p_c} = R \tag{2}$$

$$\bar{\sigma} = \sigma - \bar{\alpha}, \quad \bar{p} = p - p_{\bar{\alpha}}, \quad \bar{q} = q - q_{\bar{\alpha}} \tag{3}$$

$$\bar{\alpha} = \mathbf{c} - R\mathbf{c} \tag{4}$$

$$p_{\bar{\alpha}} = \frac{1}{3}\text{tr}(\bar{\alpha}), \quad q_{\bar{\alpha}} = \sqrt{\frac{3}{2}}\|\bar{\alpha} - p_{\bar{\alpha}}\delta\| \tag{5}$$

$$\hat{p} = \frac{1}{3}\text{tr}(\hat{\sigma}), \quad \hat{q} = \sqrt{\frac{3}{2}}\|\hat{\sigma} - \hat{p}\delta\| \tag{6}$$

where $\bar{\alpha}$ denotes the position of subloading surface, $p_{\bar{\alpha}}$ and $q_{\bar{\alpha}}$ denote the projections of $\bar{\alpha}$ on the p and q axes, respectively; $\bar{\sigma}$ denotes the stress observed from subloading surface, \bar{p} and \bar{q} are the mean stress and deviatoric stress of $\bar{\sigma}$, respectively; $\hat{\sigma}$ denotes the conjugate stress of σ on the normal-yield surface, \hat{p} and \hat{q} are the mean stress and deviatoric stress of $\hat{\sigma}$, respectively. For Cam-clay models, in particular, the size of normal-yield surface can be represented by p_c (i.e., preconsolidation pressure), and the size of subloading surface can be represented by Rp_c .

Functions of normal-yield surface and subloading surface. According to the work of Yu^{7,20}, the stress-state relation for soils can be given as:

$$\left(\frac{\eta}{M}\right)^n = 1 - \frac{\xi}{\xi_R} \tag{7}$$

$$\xi = \nu + \lambda \ln p - \Gamma \tag{8}$$

$$\xi_R = (\lambda - \kappa) \ln r \tag{9}$$

where $\eta = q/p$ is stress ratio, ξ and ξ_R are the state parameter and positive reference state parameter, respectively; λ, Γ are the well-known Cam-clay parameters; n and r are the material parameters jointly controlling the shape of yield surface. M denotes the slope of critical state line.

By substituting Eqs. (2)–(6) into Eq. (7), the normal-yield function \hat{f} and subloading function \bar{f} in general stress space can be defined as:

$$\hat{f} = \left(\frac{\hat{q}}{M\hat{p}}\right)^n + \frac{\ln(\hat{p}/p_c)}{\ln r} = 0 \tag{10}$$

$$\bar{f} = \left(\frac{q - q_{\bar{\alpha}}}{M(p - p_{\bar{\alpha}})}\right)^n + \frac{\ln[(p - p_{\bar{\alpha}})/Rp_c]}{\ln r} = 0 \tag{11}$$

It should be noted that subloading surface coincides with the normal-yield surface when $R = 1$. In this case, the subloading function becomes identical to the normal-yield function, and the subloading surface model exhibits a response similar to the conventional plasticity model.

Elastic behaviour. In general stress space, the elastic stress–strain relation can be given as:

$$\Delta\sigma = \mathbf{E} : \Delta\mathbf{e}^e = \mathbf{E} : (\Delta\mathbf{e} - \Delta\mathbf{e}^p) \tag{12}$$

$$\mathbf{E} = \left(K - \frac{2}{3}G\right)\delta \otimes \delta + 2GI \tag{13}$$

where $\Delta\sigma$ is stress increment; $\Delta\mathbf{e}, \Delta\mathbf{e}^e, \Delta\mathbf{e}^p$ are the total, elastic and plastic strain increments, respectively; \mathbf{E} denotes the elastic stiffness matrix; \mathbf{I} is a fourth-order symmetric identity tensor; K and G denote the bulk and shear modulus, respectively. It should be noted that the elastic behaviour of granular materials is non-linear and depend on the stress level. There are two types of formulations are widely adopted to describe the non-linear elastic behaviour of granular materials, i.e., hypoelasticity^{18,20,38,41,42} and hyperelasticity^{43–48} formulations. Under the framework of hypoelasticity, K and G related to the mean stress p can be defined as:

$$K = \frac{\nu_0 p}{\kappa} \tag{14}$$

$$G = \frac{3(1 - 2\mu)}{2(1 + \mu)}K \tag{15}$$

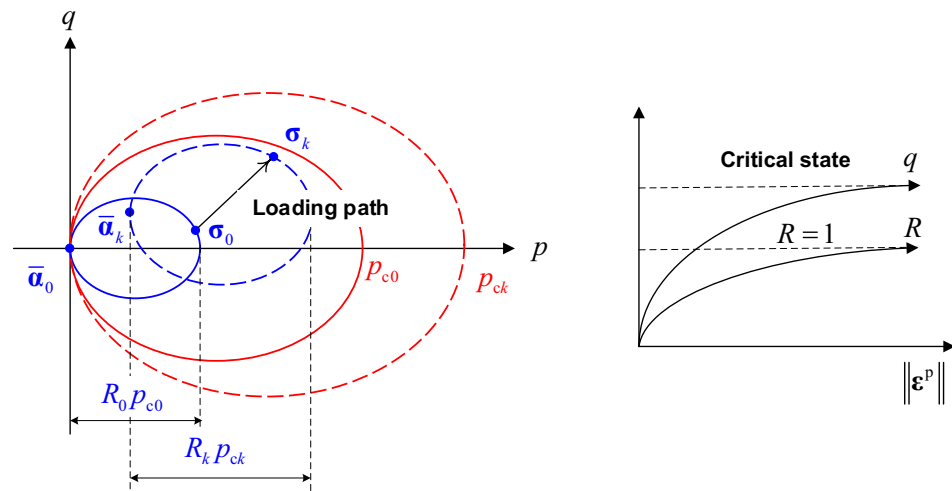


Figure 2. Schematic representation of the evolution law of subloading surface.

where κ denotes the slope of swelling line in $v - \ln p$ space; μ denotes the Poisson's ratio, v_0 denotes initial value of specific volume.

Dilatancy rule. It is well known that the associated flow rule adopted by Cam-clay would lead to an over-prediction of shear strain for soils subjected to normal compression⁴⁹. Therefore, the dilatancy rule of CASM-kII follows the relation suggested by Rowe⁵⁰:

$$D = \frac{\Delta \varepsilon_v^p}{\Delta \varepsilon_q^p} = \frac{9(M - \bar{\eta})}{9 + 3M - 2M\bar{\eta}} \tag{16}$$

where D is dilatancy rate; $\Delta \varepsilon_v^p$ and $\Delta \varepsilon_q^p$ are the volume component and shear component of plastic strain rate, respectively; $\bar{\eta} = \bar{p}/\bar{q}$ is the stress ratio on subloading surface.

Plastic flow rule. The plastic potential function of subloading surface can be obtained by integrating the Rowe's relationship:

$$g = 3M \ln \frac{\bar{p}}{\beta} + (3 + 2M) \ln(2\bar{\eta} + 3) - (3 - M) \ln(3 - \bar{\eta}) = 0 \tag{17}$$

where β is the size parameter.

Therefore, the plastic strain increment can be given as:

$$\Delta \varepsilon^p = \Delta \Lambda \bar{\mathbf{L}} = \Delta \Lambda \frac{\partial g}{\partial \bar{\boldsymbol{\sigma}}} \tag{18}$$

where $\Delta \Lambda$ and $\bar{\mathbf{L}}$ denote the magnitude and direction of plastic strain increment, respectively. According to Eqs. (11) and (18), it should be noted that the yield properties and plastic flow of CASM-kII are applied to the subloading surface instead of the normal-yield surface, which is different from the traditional elastoplastic model.

Hardening rule. The hardening rule of the subloading surface are controlled by $\bar{\alpha}$, R and p_c , and the isotropic hardening rule of the normal-yield surface is described by isotropic hardening parameter p_c , as illustrated in Fig. 2. The size of subloading surface is controlled by both p_c and R , similar to the Cam-clay plasticity, the variable p_c is controlled by the increment of plastic volumetric strain:

$$\Delta p_c = \theta p_c \Delta \varepsilon_v^p, \quad \theta = \frac{v_0}{\lambda - \kappa} \tag{19}$$

$$\Delta \varepsilon_v^p = \Delta \Lambda \text{tr}(\bar{\mathbf{L}}) \tag{20}$$

Integrating Eqs. (18) and (19) over a finite time increment yields the following alternative incremental hardening laws:

$$p_{ck+1} = p_{ck} \exp(\theta \Delta \varepsilon_v^p) \tag{21}$$

Step	Brief description
1	Input the variables σ_k, \mathbf{c}_k and p_{ck} at the end of step k
2	Set the initial value $R_k^i = R_k^0 = R_{k+1}$ and the tolerance error $TOL = 1e - 6$, where superscript i indicates the number of iterations
3	Calculate the stress on the subloading surface and its components on the subloading surface $\bar{\sigma}_k = \sigma_k - (1 - R_k^i)\mathbf{c}_k$ $\bar{p}_k = \frac{1}{3} \text{tr}(\bar{\sigma}_k), \bar{q}_k = \sqrt{\frac{3}{2}} \ \bar{\sigma}_k - \bar{p}_k \delta\ $
4	Compute the subloading surface function $f_k = \left(\frac{q_k}{M p_k}\right) + \frac{\ln(p_k / \sigma_k p_{ck})}{\ln r}$
5	Compute the derivative of subloading surface function with respect to R_k^i $\frac{\partial f_k}{\partial R_k^i} = n \frac{q_k}{M p_k^{n+1}} (q_{sk} \bar{p}_k - p_{sk} \bar{q}_k) + \frac{1}{\ln r} \left(\frac{p_{sk}}{p_k} - \frac{1}{r}\right)$ where $p_{sk} = \frac{1}{3} \text{tr}(\mathbf{c}_k), q_{sk} = \sqrt{\frac{3}{2}} \ \mathbf{c}_k - p_{sk} \delta\ $
6	Update the normal-yield ratio by: $R_k^{i+1} = R_k^i - \frac{f_k}{\partial f_k / \partial R_k^i}$
7	If $ f_k^{i+1} < TOL, R_k = R_k^{i+1}$, and go to next step $k + 1$, else back to step 3

Table 1. The numerical calculation procedure of R by the Newton–Raphson method.

Considering that the stress approaches the normal-yield surface progressively, i.e., the subloading surface approaches the yield surface gradually during the plastic loading procedure, the rate of R can be defined as:

$$\Delta R = U \|\Delta \mathbf{e}^P\| = \Delta \Lambda U \|\bar{\mathbf{L}}\|, \text{ when } \Delta \mathbf{e}^P \neq \mathbf{O} \tag{22}$$

where \mathbf{O} is a two-order zero tensor; U is a monotonically decreasing function of the normal-yield ratio R , and it must satisfy the following rules:

$$\begin{cases} U = +\infty & \text{for } R = 0 \\ U > 0 & \text{for } R \in (0, 1) \\ U = 0 & \text{for } R = 1 \\ U < 0 & \text{for } R > 1 \end{cases} \tag{23}$$

There are many mathematical expressions of U that can satisfy Eq. (23), and here we adopt a simple one:

$$U = -h_m \ln(R) \tag{24}$$

where h_m is a new material constant controlling the rate of subloading surface that approaches to the normal-yield surface.

It should be noted that during the elastic unloading process (the loading criterion will be given in the next section), R must be calculated according to the nonlinear Eq. (11) formed by current known values of $\sigma, \bar{\alpha}$ and p_c , because Eq. (22) only holds for the plastic loading process. However, the subloading equation is of high-order (n -order), which makes it impractical to obtain the analytical solution of R . Hence, the Newton–Raphson method might be appropriate for calculation of R . The complete calculation procedure of R during elastic unloading process is listed in Table 1.

Besides, it should be noted that the similarity center should be located inside the normal-yield surface during the whole loading process. Following the concept of subloading surface, the similarity center surface can be defined as follows:

$$f(\mathbf{c}) = R_{cen} p_c \tag{25}$$

where the similarity center surface passes through the similarity center point and is similar to the normal-yield surface in terms of stress space origin. R_{cen} is the ratio of the size of the similarity center surface to the normal-yield surface. To make certain that the similarity center lies inside the limit surface, i.e., $f(\mathbf{c}) = r_c p_c$, the following inequality must hold:

$$0 \leq f(\mathbf{c}) \leq r_c p_c, \quad 0 \leq R_{cen} \leq r_c \tag{26}$$

where r_c ($0 < r_c < 1$) is a new material constant designating the maximum value of R_{cen} . Besides, the similarity center surface is unable to be bigger than the normal-yield surface, by using the properties of homogeneous function, the closure condition of similarity center can be obtained:

$$\frac{\partial f(\mathbf{c})}{\partial \mathbf{c}} : \left[\Delta \mathbf{c} - \frac{\Delta p_c}{p_c} \mathbf{c} \right] \leq 0, \text{ when } 0 \leq R_{cen} \leq r_c \tag{27}$$

Then, it can be assumed that the rate of similarity center can be written as:

$$\Delta \mathbf{c} = \frac{\Delta p_c}{p_c} \mathbf{c} + h_c \|\Delta \mathbf{e}^P\| \left(\frac{\bar{\sigma}}{R} - \frac{\mathbf{c}}{r_c} \right) \tag{28}$$

where h_c is a new material constant controlling the evolution rate of similarity center.

By Substituting Eq. (28) into Eq. (4), the rate of $\bar{\alpha}$ is given by:

$$\Delta\bar{\alpha} = (1 - R) \left\{ h_c \|\Delta\boldsymbol{\varepsilon}^p\| \left(\frac{\bar{\sigma}}{R} - \frac{\mathbf{c}}{r_c} \right) + \frac{\Delta p_c}{p_c} \mathbf{c} \right\} - \mathbf{c} \Delta R \quad (29)$$

Consistency condition and plastic modulus. Different from the traditional elastoplastic model, the consistency condition of subloading surface model is applied to the subloading function instead of normal-yield function¹³. According to Eq. (11), the consistency condition of subloading function can be given as:

$$\bar{\mathbf{N}} : \Delta\bar{\sigma} + \bar{f}_R \Delta R + \bar{f}_{p_c} \Delta p_c = 0 \quad (30)$$

$$\bar{\mathbf{N}} = \frac{\partial \bar{f}}{\partial \bar{\sigma}}, \quad \bar{f}_R = \frac{\partial \bar{f}}{\partial R}, \quad \bar{f}_{p_c} = \frac{\partial \bar{f}}{\partial p_c} \quad (31)$$

Substituting Eqs. (12), (18), (19), (22) and (29) into Eq. (30), the plastic multiplier can be given as:

$$\Delta\Lambda = \frac{\bar{\mathbf{N}} : \mathbf{E} : \Delta\boldsymbol{\varepsilon}}{K_p + \bar{\mathbf{N}} : \mathbf{E} : \bar{\mathbf{L}}} \quad (32)$$

where K_p is plastic modulus. According to the consistency condition of subloading function, the mathematical expression of K_p is written as:

$$K_p = \bar{\mathbf{N}} : (1 - R) \left\{ \theta \text{tr}(\bar{\mathbf{L}}) \mathbf{c} + h_c \|\bar{\mathbf{L}}\| \left(\frac{\bar{\sigma}}{R} - \frac{\mathbf{c}}{r_c} \right) \right\} - \bar{\mathbf{N}} : \mathbf{c} U \|\bar{\mathbf{L}}\| + \frac{1}{\ln r} \left\{ \frac{U}{R} \|\bar{\mathbf{L}}\| - \theta \text{tr}(\bar{\mathbf{L}}) \right\} \quad (33)$$

By substituting Eq. (32) into Eq. (12), the elastoplastic stiffness matrix \mathbf{E}^{ep} can be defined as:

$$\mathbf{E}^{\text{ep}} = \mathbf{E} - \varsigma \frac{\mathbf{E} : \bar{\mathbf{L}} \otimes \bar{\mathbf{N}} : \mathbf{E}}{K_p + \bar{\mathbf{N}} : \mathbf{E} : \bar{\mathbf{L}}} \quad (34)$$

where ς is the loading index, and the loading criterion¹⁵ is given as:

$$\begin{cases} \bar{\mathbf{N}} : \mathbf{E} : \Delta\boldsymbol{\varepsilon} > 0, \varsigma = 1, \text{ Loading} \\ \bar{\mathbf{N}} : \mathbf{E} : \Delta\boldsymbol{\varepsilon} \leq 0, \varsigma = 0, \text{ Unloading} \end{cases} \quad (35)$$

Numerical implementation scheme. Existing numerical implementation schemes of the constitutive models are generally classified as backward Euler^{51–54} and forward Euler^{55–57} schemes. The backward Euler scheme with the return-mapping technique is accurate because the resulting stress automatically satisfy the yield function to a specified tolerance. However, this backward Euler method requires the second derivatives of the yield and the plastic potential functions, which makes it difficult to the implement for complex constitutive relations⁵⁸. Compared with back Euler scheme, forward Euler scheme have the advantage of being more straightforward to implement. Therefore, the forward Euler scheme with automatic substepping and error control is adopted in this study because its simplicity and efficiency. The forward Euler scheme with automatic substepping and error control can divide the loading step into several substeps according to the local computational accuracy required. It is assumed that the strain increment input by the analysis system is $\Delta\boldsymbol{\varepsilon}_{k+1}$ at step k to step $k + 1$, this original increment may be too large and leads to excessive error sometimes. To avoid the drift of yield surface and improve computational precision, it is necessary to divide this increment into a series of parts (substeps) to satisfy the local tolerance error. The complete load integration algorithm may be implemented as Table 2:

Model constants

The newly proposed model CASM-kII requires ten material parameters ($\Gamma, \lambda, \kappa, \mu, M, r, n, h_m, h_c$ and r_c) and initial values of the of the internal hardening variables (p_{c0}, R_0 and $\bar{\alpha}_0$). The roles of each constant are listed in Table 3. $\Gamma, \lambda, \kappa, \mu$ and M are the well-known constants in Cam-clay plasticity, which are called the “basic constants”. r and n are called yield constants because they control the shape of normal yield surface. The detailed calibration procedure of the basic and yield constants can be referred to the work of Yu^{7,20}, Rios et al.¹² and Navarro et al.⁵⁹. h_m, h_c and r_c are the newly introduced material parameters used to control the evolution rule of subloading surface, which called “Hardening constants” in this study. The variable p_{c0} can be determined by the preconsolidation pressure. As shown in Fig. 2, the initial value of the position tensor can be set as $\bar{\alpha}_0 = \mathbf{O}$ for initial isotropy¹⁵. Once p_{c0} and $\bar{\alpha}_0$ are known, R_0 can be easily obtained from the subloading function of Eq. (11) as follows:

$$R_0 = \frac{\bar{p}_0}{p_{c0}} \exp \left[\left(\frac{\bar{q}_0}{M\bar{p}_0} \right)^n \ln r \right] \quad (36)$$

where \bar{p}_0 and \bar{q}_0 are the initial mean stress and initial deviatoric stress on subloading surface, respectively.

As suggested by Hashiguchi¹⁵, h_m can be determined from the stress–strain curve in the subyield state while h_c and r_c can be determined from the stress–strain curve in cyclic loading. Before using CASM-kII to predict the mechanical response of a practical engineering problem, it is instructive to investigate the influence of hardening

Step	Brief description
1	Input initial variables $\sigma_k, \epsilon_k, c_k, p_{ck}, R_k$ and the strain increment $\Delta \epsilon_{k+1}$
2	Set the pseudo time $T = 0, \Delta T = 1$ and the tolerance error $STOL = 1e - 6$
3	Calculate the first trial elasto-plastic stiffness matrix $E_1^{ep} \{ \sigma_k, c_k, p_{ck}, R_k \}$ by substituting the initial variables into Eq. (34)
4	Compute the subincrement according to $\Delta \epsilon_{k+1}^{sub} = \Delta T \times \Delta \epsilon_{k+1}$
5	Calculate the first trial stress increment $\Delta \sigma_1 = E_1^{ep} : \Delta \epsilon_{k+1}^{sub}$ and update the first trial state variables c_1, p_{c1} and R_1 related to plastic deformation
6	Compute the second trial elastoplastic stiffness matrix $E_2^{ep} \{ \sigma_1, c_1, p_{c1}, R_1 \}$ by substituting the first trial variables into Eq. (34)
7	Calculate the second trial stress increment $\Delta \sigma_2 = E_2^{ep} : \Delta \epsilon_{k+1}^{sub}$
8	Calculate the average stress increment $\Delta \sigma_{k+1} = \frac{1}{2} (\Delta \sigma_1 + \Delta \sigma_2)$
9	Compute the relative local error $LE = \frac{\ \frac{1}{2} (\Delta \sigma_1 - \Delta \sigma_2) \ }{\ \sigma_k + \Delta \sigma_{k+1} \ }$
10	If $LE > STOL$, the size of this substep is too large and a smaller pseudo time needs to be found: $\rho = \max \{ 0.9 \sqrt{STOL/LE}, 0.1 \}$, $\Delta T = \max \{ \rho \Delta T, 0.001 \}$, then return to step 4 Else, go to next step
11	Compute the size of next substep $\rho = \min \{ 0.9 \sqrt{STOL/LE}, 1.1 \}$ If the above equation is rejected, then $\rho = \min \{ \rho, 0.9 \}$ Update the pseudo time $T = T + \Delta T, \Delta T = \rho \Delta T$
12	Recalculate the pseudo time to ensure the size of next substep is bigger than that of minimum step and is not bigger than 1, the following conditions must be applied $\Delta T = \max \{ \Delta T, 0.001 \}, \Delta T = \min \{ \Delta T, 1 - T \}$
13	While $T = 1$ end this iterative calculation and output the Jacobi stiffness matrix C_{k+1} to the finite element routine for the global equilibrium iterations. The Jacobi stiffness matrix can be derived from the same procedure in solving the elastoplastic matrix ⁵⁸ : $C_{k+1} = E_{k+1}^{ep} \{ \sigma_{k+1}, c_{k+1}, p_{ck+1}, R_{k+1} \}$

Table 2. Flowchart of the integration scheme.

Category	Symbol	Description
Basic constants	Γ	Intersection of critical state line with $p = 1$ kPa line in $e - \ln p$ space
	λ	Slope of compression line in $e - \ln p$ space
	κ	Slope of swelling line in $e - \ln p$ space
	μ	The Poisson's ratio
	M	Slope of critical state line in $p - q$ space
Yield constants	r	Controls the shape of normal-yield surface
	n	Controls the shape of normal-yield surface
Hardening constants	h_m	Controls the evolution rate of the size of subloading surface
	h_c	Controls the evolution rate of the position of subloading surface
	r_c	Controls the maximum size of similarity center surface
Initial internal hardening variables	p_{c0}	Initial value of preconsolidation pressure
	R_0	Initial value of normal-yield ratio
	$\bar{\alpha}_0$	Initial position of subloading surface

Table 3. Model constants in CASM-kII.

constants on the predicted mechanical properties of soils under drained (or undrained) monotonic loading (or cyclic loading) conditions. In this study, a sensitivity study is carried out to check the influences of these three new parameters (h_m, h_c and r_c) on the mechanical response of soils in over-consolidation and cyclic loading conditions. The basic and yield material constants are set as $\Gamma = 2.59, \lambda = 0.15, \kappa = 0.05, \mu = 0.3, M = 1, r = 2.718, n = 1.6$ while the hardening parameters h_m, h_c and r_c are variables. It is assumed that the samples used in the test are isotropically consolidated with $p_{c0} = 100$ kPa, $v_0 = 2$ and $\bar{\alpha}_0 = \mathbf{O}$. In the monotonic loading test under drained and undrained conditions, the OCRs of the samples are set to 4 and 8 ($R_0 = 0.25$ when $\text{OCR} = 4, R_0 = 0.125$ when $\text{OCR} = 8$). In the cyclic loading test under drained and undrained conditions, the samples are slightly over-consolidated ($\text{OCR} = 1.5, R_0 = 0.667$) and a two-way cyclic loading ($q = \pm 30$ kPa) is applied.

As illustrated in Fig. 3, the value of h_m significantly affects the mechanical properties (such as stress-strain relation, stress path, shear dilatancy and the normal-yield ratio evolution) of over-consolidated samples under monotonic loading. The sample reaches the critical state earlier (drained condition) and demonstrates a larger peak strength (undrained condition) with a bigger value of h_m under plastic loading process.

Figure 4 shows the performances of different h_c and r_c under undrained cyclic loading tests. It can be found the hysteresis loop increases quicker (softening behaviour) with smaller values of h_c and r_c . As illustrated in Fig. 4b,d, the normal-yield ratio R varies like a butterfly with the loading and unloading process. As shown in

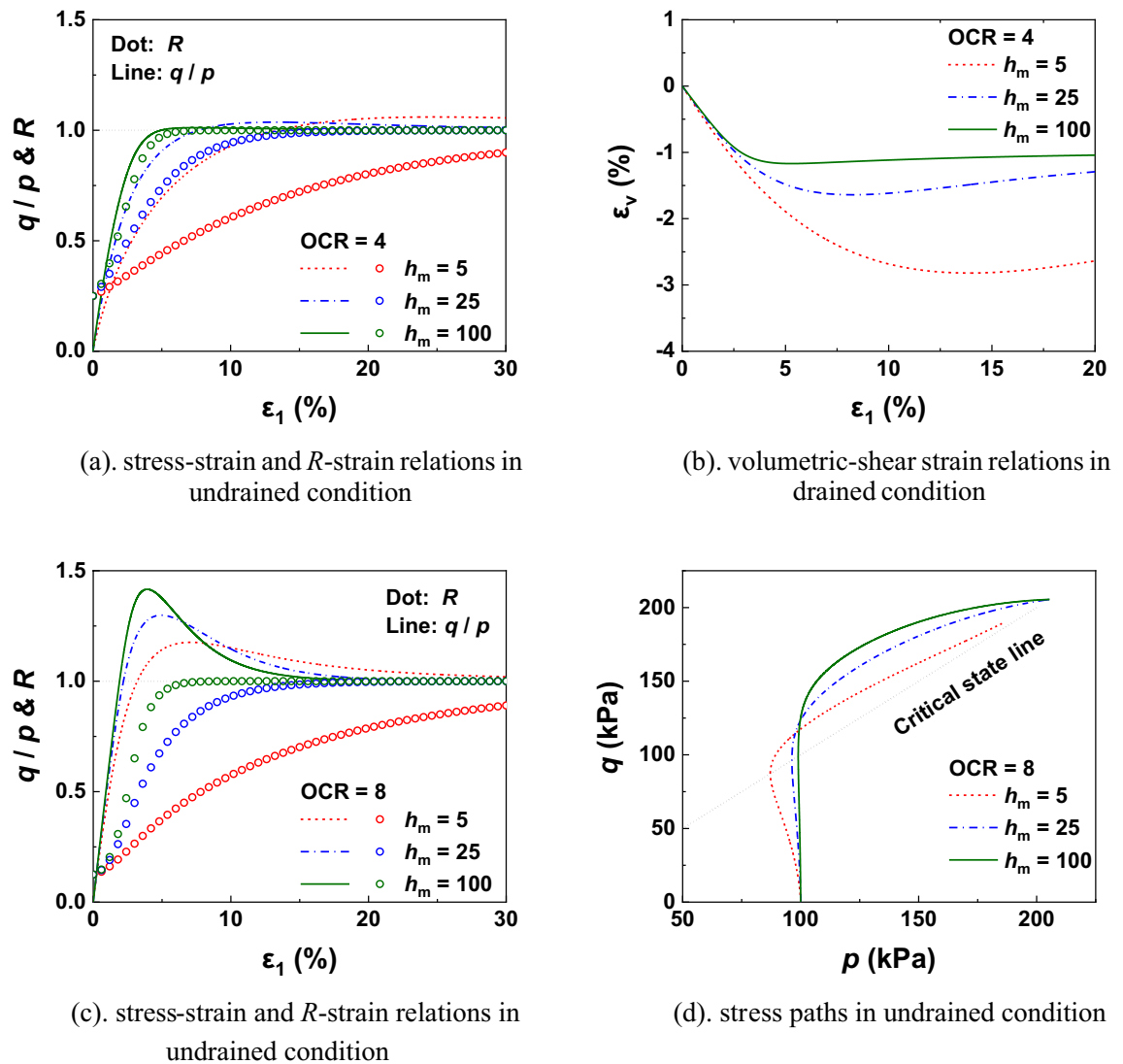


Figure 3. Drained and undrained simulations with different values of h_m in monotonic loading process.

Fig. 5, the performances of different h_c and r_c under drained cyclic loading tests is checked. The accumulated plastic deformation and shear dilatancy under drained conditions demonstrate larger with smaller values of h_c and r_c because the rate of reverse plastic flow is slower at this time.

Numerical simulations

In order to assess the performance of this newly proposed CASM-kII in monotonic and cyclic loading conditions, the experiment data of Jiangxi clay, Boston blue clay, Toyoura sand and Commercially available clay are used in this study. The values of the basic constants, yield constants and initial values of internal hardening variables used in the simulations are determined through the reported results and recommended values in previous study^{11,21,60–62}, while the hardening parameters are determined through the methods in previous section. The material constants of these four samples are listed in Table 4.

Drained triaxial tests. The drained triaxial tests of Jiangxi clay was proposed by Hu et al.⁶² with these samples are applied consolidation confining pressure to 98 kPa, 196 kPa and 784 kPa in triaxial apparatus. These samples had a height of 80 mm and a diameter of 39.1 mm. In order to prepare samples with over consolidation ratios of 1, 2 and 8, the confining pressure was unloaded to 98kpa step by step. As illustrated in Fig. 6, CASM-kII can accurately simulate the stress–strain and deformation characteristics in normally and over-consolidation conditions. In particular, the newly proposed model is found to be relatively capable of capturing the dilatancy behaviour of the overconsolidated clay observed in the laboratory tests.

Undrained triaxial tests. The measured data of Boston blue clay of Pestana et al.⁶⁰ is used here to validate the prediction ability of CASM-kII for the mechanical properties of overconsolidated clays under undrained loading process, with the pre-consolidation pressure set to 196 kPa and the over-consolidation ratios set to

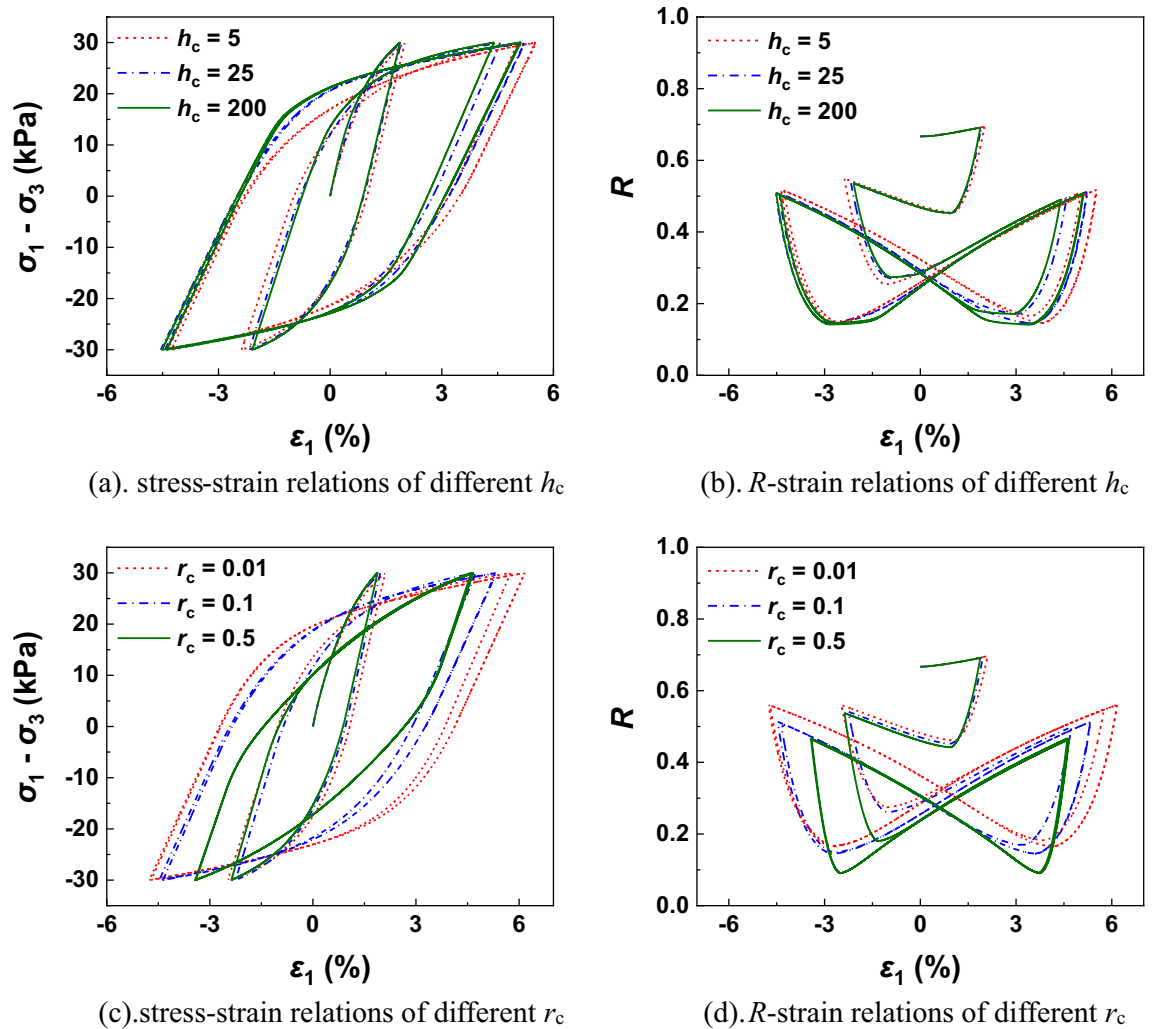


Figure 4. Undrained simulations with different values of h_c and r_c in cyclic loading process.

OCR=1, 2, 8. Figure 7 shows that the agreement between measured data and simulation data of both stress–strain relation and stress paths is satisfactory. Besides, CASM-kII is able to predict the smooth stress–strain curves in over-consolidation conditions, whilst the original CASM fails to predict⁹.

Then, the experimental data of Toyoura sand observed by Verdugo and Ishihara⁶³ is used here to evaluate the prediction ability of CASM-kII to capture the behaviour of sands. The undrained tests of Toyoura sand were conducted under very high confining pressures ($p = 1, 2, 3$ MPa) with same void ratio $e_0 = 0.71$. The initial values of internal variables can be referred to the work of Zhang et al.⁶¹. As shown in Fig. 8, the results simulated by CASM-kII coincide well with the experimental results quantitatively and qualitatively. Under the same void ratio, the sands behave the properties of loose sands when the confining stress is large, while the sands behave the properties of dense sands when the confining stress is small. Such a phenomenon is called as “confining-stress dependency of sand”⁶⁴.

Cyclic loading tests. To verify the applicability of the new model under cyclic loading conditions, the experiment data observed by Li and Meissner²¹ is used here. The material constants and initial conditions of these samples can be found in Table 4. These cyclic tests are stress-controlled with the half amplitude of the deviatoric stress $q = 116$ kPa. Figure 9 shows the observed data and the simulation data, the deviatoric stress is plotted against the axial strain while the excess pore water pressure (Δu) is plotted against the number of cycles, where CASM-kII can describe the behaviour of undrained commercially available clay under cyclic loading conditions.

Conclusions

In this paper, a modified unified critical state model (called CASM-kII) to predict the mechanical properties of both clays and soils under over-consolidation and cyclic loading conditions is developed on the basis of original CASM model and subloading surface concept. Through the introduction of subloading surface, this newly proposed model is able to describe the plastic deformation inside the yield surface and the reverse plastic flow, and is thus expected to accurately capture the over-consolidated and cyclic behaviours. CASM-kII is numerical implemented by the using of the forward Euler scheme with automatic substepping and error control. Then,

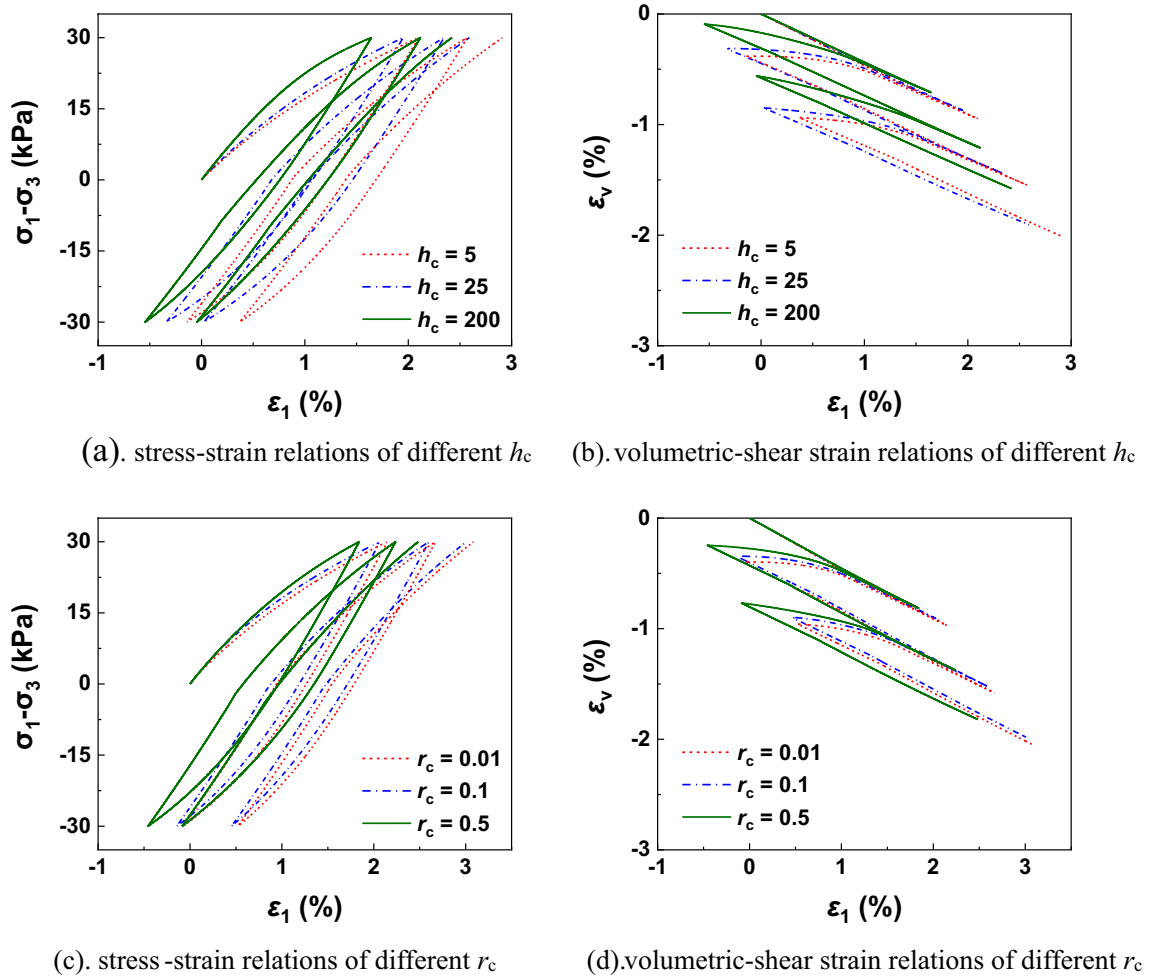


Figure 5. Drained simulations with different values of h_c and r_c in cyclic loading process.

	Jiangxi clay	Boston blue clay	Toyoura sand	Commercially available clay
Basic constants	$\Gamma = 2.255$	$\Gamma = 2.501$	$\Gamma = 2.067$	$\Gamma = 2.134$
	$\lambda = 0.095$	$\lambda = 0.184$	$\lambda = 0.05$	$\lambda = 0.173$
	$\kappa = 0.018$	$\kappa = 0.036$	$\kappa = 0.0064$	$\kappa = 0.05$
	$\mu = 0.3$	$\mu = 0.3$	$\mu = 0.3$	$\mu = 0.3$
	$M = 1.36$	$M = 1.35$	$M = 1.3$	$M = 0.772$
Yield constants	$r = 2.2$	$r = 2.718$	$r = 12$	$r = 2.718$
	$n = 3.5$	$n = 1.8$	$n = 2$	$n = 2$
Hardening constants	$h_m = 95$	$h_m = 40$	$h_m = 80$	$h_m = 750$
	$h_c = 10$	$h_c = 25$	$h_c = 55$	$h_c = 35$
	$r_c = 0.95$	$r_c = 0.9$	$r_c = 0.7$	$r_c = 0.95$
Initial internal variables	$v_0 = 1.88$	$v_0 = 2.01$	$v_0 = 1.71$	$v_0 = 2.15$
	$\bar{\alpha}_0 = 0$	$\bar{\alpha}_0 = 0$	$\bar{\alpha}_0 = 0$	$\bar{\alpha}_0 = 0$
	OCR=1:	OCR=1:	$p = 1$ MPa:	$p_{c0} = 450$ kPa
	$p_{c0} = 98$ kPa, $R_0 = 1$	$p_{c0} = 196$ kPa, $R_0 = 1$	$p_{c0} = 8$ MPa, $R_0 = 0.125$	$R_0 = 1$
	OCR=2:	OCR=2:	$p = 2$ MPa:	
	$p_{c0} = 196$ kPa, $R_0 = 0.5$	$p_{c0} = 392$ kPa, $R_0 = 0.5$	$p_{c0} = 10$ MPa, $R_0 = 0.2$	
	OCR=8:	OCR=8:	$p = 3$ MPa: $p_{c0} = 10.5$ MPa, $R_0 = 0.286$	
$p_{c0} = 784$ kPa, $R_0 = 0.125$	$p_{c0} = 1568$ kPa, $R_0 = 0.125$			

Table 4. The material constants of different samples.

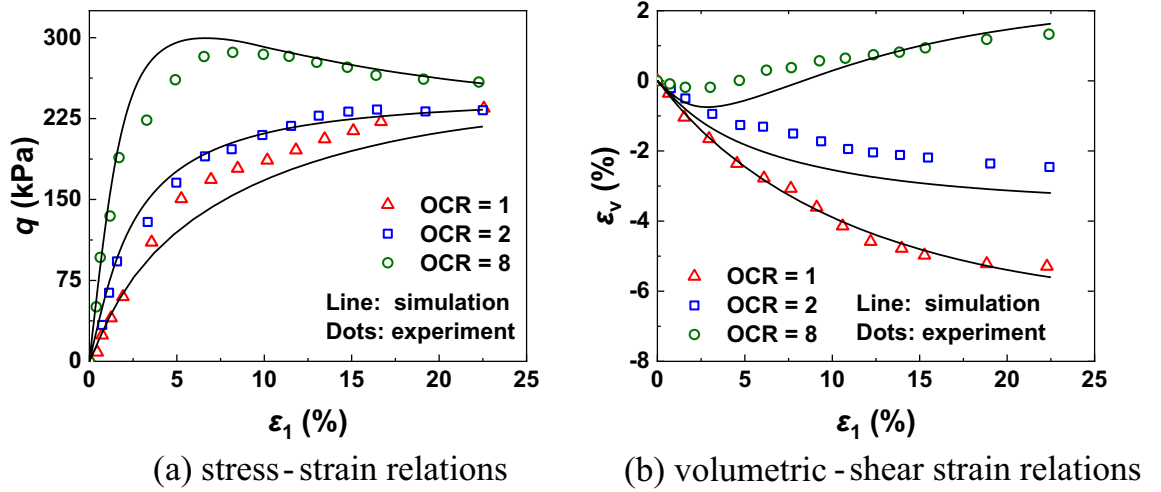


Figure 6. Model predictions and experiment results of Jiangxi clay under drained conditions.

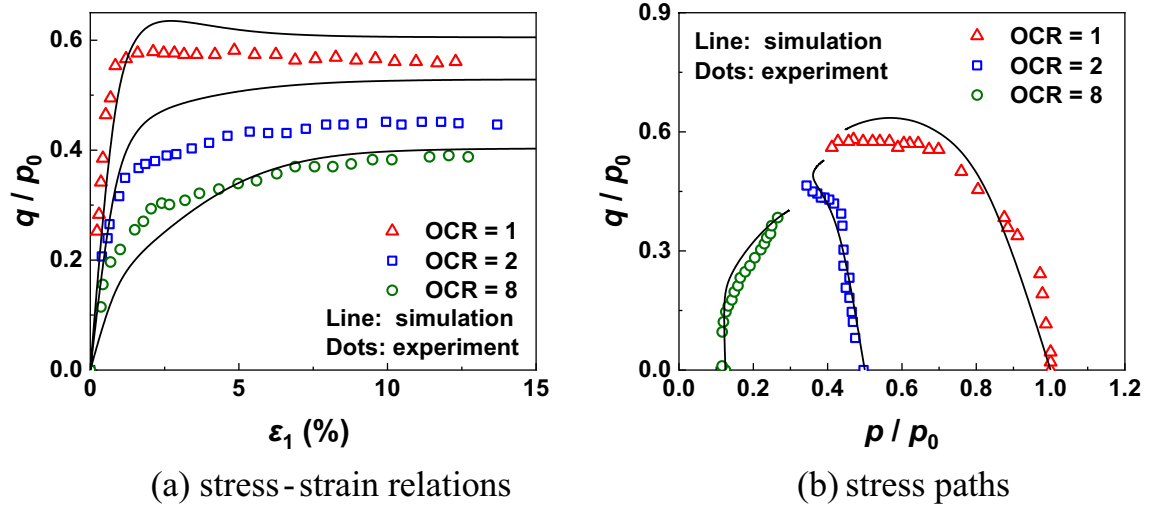


Figure 7. Model predictions and experiment results of Boston blue clay under undrained conditions.

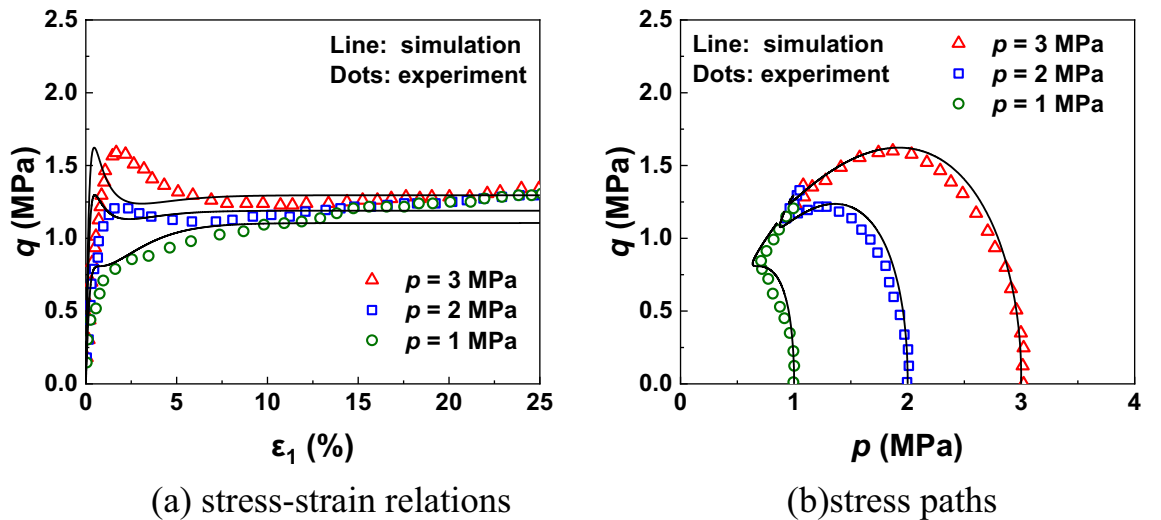


Figure 8. Model predictions and experiment results of Toyoura sand under undrained conditions.

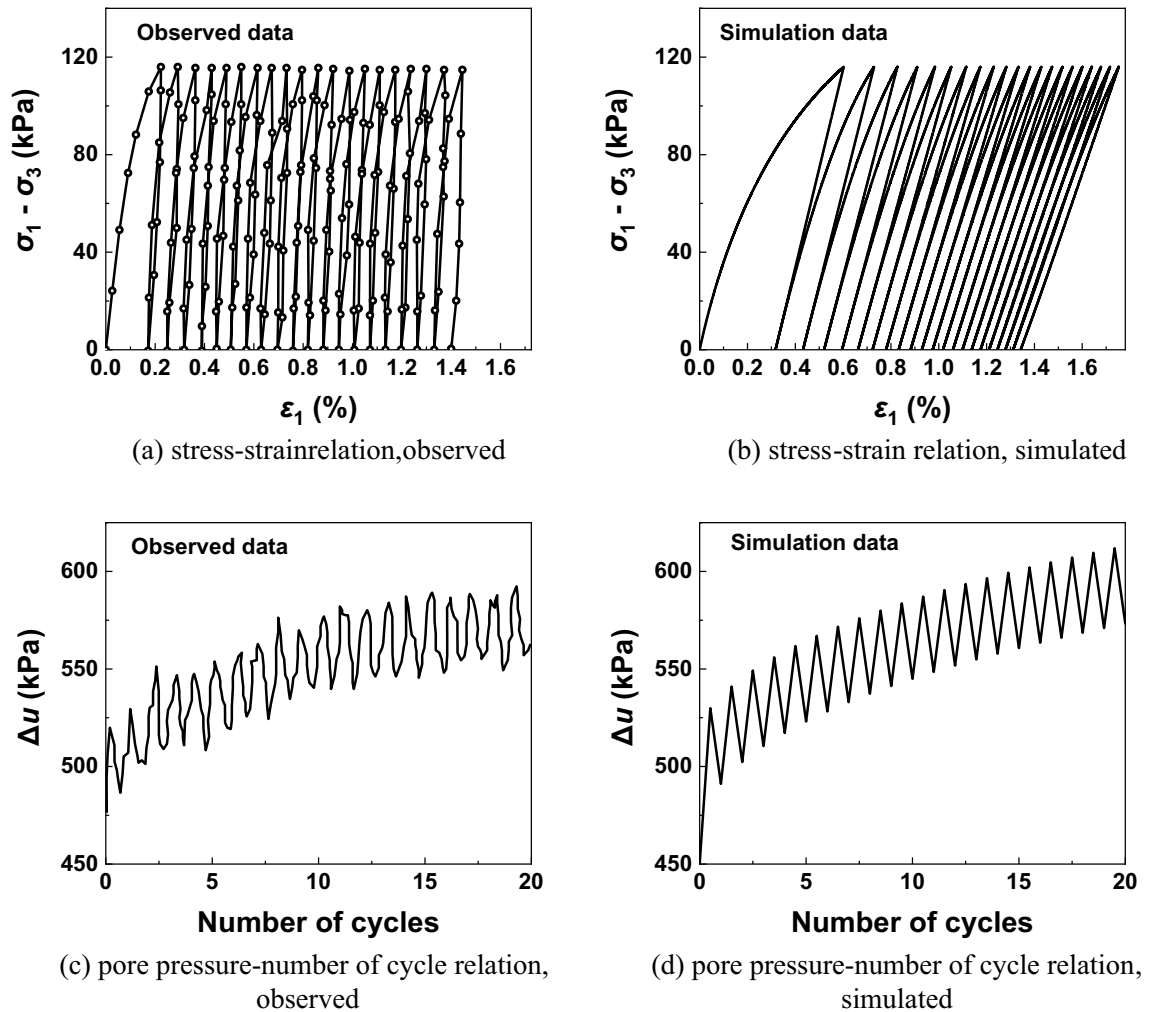


Figure 9. Model predictions and experiment results of Commercially available clay under undrained conditions.

a sensitivity study is carried out to check the influences of these three new parameters (h_m , h_c and r_c) on the mechanical response of soils in over-consolidation and cyclic loading conditions. Through the comparisons of experimental data and simulated results, it is found that CASM-kII performs well in the simulations of both clays and sands in over-consolidation and cyclic loading conditions.

Data availability

Some or all data, models, or code that support the findings of this study are available from the corresponding author upon reasonable request.

Received: 31 July 2022; Accepted: 16 December 2022

Published online: 21 February 2023

References

1. Roscoe, K. H. & Burland, J. B. On the generalized stress-strain behaviour of wet clay. *Eng. Plast.* 535–609, <https://trid.trb.org/view/124868> (1968).
2. Borja, R. I. & Lee, S. R. Cam-clay plasticity, part I: Implicit integration of elasto-plastic constitutive relations. *Comput. Methods Appl. Mech. Eng.* 78, 49–72. [https://doi.org/10.1016/0045-7825\(90\)90152-C](https://doi.org/10.1016/0045-7825(90)90152-C) (1990).
3. Borja, R. I., Lin, C.-H. & Montáns, F. J. Cam-Clay plasticity, Part IV: Implicit integration of anisotropic bounding surface model with nonlinear hyperelasticity and ellipsoidal loading function. *Comput. Methods Appl. Mech. Eng.* 190, 3293–3323. [https://doi.org/10.1016/S0045-7825\(00\)00301-7](https://doi.org/10.1016/S0045-7825(00)00301-7) (2001).
4. Liu, M. & Carter, J. A structured cam clay model. *Can. Geotech. J.* 39, 1313–1332. <https://doi.org/10.1139/t02-069> (2002).
5. Tamagnini, R. An extended cam-clay model for unsaturated soils with hydraulic hysteresis. *Geotechnique* 54, 223–228. <https://doi.org/10.1680/geot.2004.54.3.223> (2004).
6. Horpibulsuk, S., Liu, M. D., Liyanapathirana, D. S. & Suebsuk, J. Behaviour of cemented clay simulated via the theoretical framework of the structured cam clay model. *Comput. Geotech.* 37, 1–9. <https://doi.org/10.1016/j.compgeo.2009.06.007> (2010).
7. Yu, H. S. CASM: A unified state parameter model for clay and sand. *Int. J. Numer. Anal. Meth. Geomech.* 22, 621–653. [https://doi.org/10.1002/\(SICI\)1096-9853\(199808\)22:8%3c621::AID-NAG937%3e3.0.CO;2-8](https://doi.org/10.1002/(SICI)1096-9853(199808)22:8%3c621::AID-NAG937%3e3.0.CO;2-8) (1998).

8. Sheng, D., Sloan, S. & Yu, H. Aspects of finite element implementation of critical state models. *Comput. Mech.* **26**, 185–196. <https://doi.org/10.1007/s004660000166> (2000).
9. Khong, C. D. *Development and Numerical Evaluation of Unified Critical State Models*. University of Nottingham (2004).
10. Yang, Y. M. & Yu, H. S. A non-coaxial critical state soil model and its application to simple shear simulations. *Int. J. Numer. Anal. Meth. Geomech.* **30**, 1369–1390. <https://doi.org/10.1002/nag.531> (2006).
11. Yu, H. S., Khong, C. & Wang, J. A unified plasticity model for cyclic behaviour of clay and sand. *Mech. Res. Commun.* **34**, 97–114. <https://doi.org/10.1016/j.mechrescom.2006.06.010> (2007).
12. Rios, S., Ciantia, M., González, N., Arroyo, M. & António, V. Simplifying calibration of bonded elasto-plastic models. *Comput. Geotech.* **73**, 100–108. <https://doi.org/10.1016/j.compgeo.2015.11.019> (2016).
13. Hashiguchi, K. Subloading surface model in unconventional plasticity. *Int. J. Solids Struct.* **25**, 917–945. [https://doi.org/10.1016/0020-7683\(89\)90038-3](https://doi.org/10.1016/0020-7683(89)90038-3) (1989).
14. Hashiguchi, K. *Elastoplasticity Theory* Vol. 42 (Springer, 2009).
15. Hashiguchi, K. *Foundations of Elastoplasticity: Subloading Surface Model* (Springer, 2017).
16. Jardine, R., Symes, M. & Burland, J. The measurement of soil stiffness in the triaxial apparatus. *Geotechnique* **34**, 323–340. <https://doi.org/10.1680/geot.1984.34.3.323> (1984).
17. Hashiguchi, K., Saitoh, K., Okayasu, T. & Tsutsumi, S. Evaluation of typical conventional and unconventional plasticity models for prediction of softening behaviour of soils. *Geotechnique* **52**, 561–578. <https://doi.org/10.1680/geot.2002.52.8.561> (2002).
18. Yao, Y. P., Hou, W. & Zhou, A. N. UH model: Three-dimensional unified hardening model for overconsolidated clays. *Geotechnique* **59**, 451–469. <https://doi.org/10.1680/geot.2007.00029> (2009).
19. Wu, S., Zhou, A., Li, J., Kodikara, J. & Cheng, W.-C. Hydromechanical behaviour of overconsolidated unsaturated soil in undrained conditions. *Can. Geotech. J.* **56**, 1609–1621. <https://doi.org/10.1139/cgj-2018-0323> (2018).
20. Yu, H. S. *Plasticity and Geotechnics* Vol. 13 (Springer, 2007).
21. Li, T. & Meissner, H. Two-surface plasticity model for cyclic undrained behavior of clays. *J. Geotech. Geoenviron. Eng.* **128**, 613–626. <https://doi.org/10.1002/nag.238> (2002).
22. Hau, K. W., McDowell, G., Zhang, G. & Brown, S. The application of a three-surface kinematic hardening model to repeated loading of thinly surfaced pavements. *Granul. Matter* **7**, 145–156. <https://doi.org/10.1007/s10035-005-0199-9> (2005).
23. Yang, Y. M. & Yu, H. S. A kinematic hardening soil model considering the principal stress rotation. *Int. J. Numer. Anal. Meth. Geomech.* **37**, 2106–2134. <https://doi.org/10.1002/nag.2138> (2013).
24. Avgerinos, V., Potts, D. & Standing, J. The use of kinematic hardening models for predicting tunnelling-induced ground movements in London Clay. *Geotechnique* **66**, 106–120 (2016).
25. Stoecklin, A., Friedli, B. & Puzrin, A. M. A multisurface kinematic hardening model for the behavior of clays under combined static and undrained cyclic loading. *Int. J. Numer. Anal. Meth. Geomech.* **44**, 2358–2387. <https://doi.org/10.1002/nag.3149> (2020).
26. Cui, Y.-J., Nguyen, X.-P., Tang, A. M. & Li, X.-L. An insight into the unloading/reloading loops on the compression curve of natural stiff clays. *Appl. Clay Sci.* **83**, 343–348. <https://doi.org/10.1016/j.clay.2013.08.003> (2013).
27. Al-Tabbaa, A. *Permeability and Stress-Strain Response of Speswhite Kaolin* (University of Cambridge, 1988).
28. Asaoka, A., Nakano, M. & Noda, T. Superloading yield surface concept for highly structured soil behavior. *Soils Found.* **40**, 99–110. https://doi.org/10.3208/sandf.40.2_99 (2000).
29. Zhang, F., Ye, B., Noda, T., Nakano, M. & Nakai, K. Explanation of cyclic mobility of soils: Approach by stress-induced anisotropy. *Soils Found.* **47**, 635–648. <https://doi.org/10.3208/sandf.47.635> (2007).
30. Dafalias, Y. F. An anisotropic critical state soil plasticity model. *Mech. Res. Commun.* **13**, 341–347. [https://doi.org/10.1016/0093-6413\(86\)90047-9](https://doi.org/10.1016/0093-6413(86)90047-9) (1986).
31. Dafalias, Y. F., Manzari, M. T. & Akaishi, M. A simple anisotropic clay plasticity model. *Mech. Res. Commun.* **29**, 241–245. [https://doi.org/10.1016/S0093-6413\(02\)00252-5](https://doi.org/10.1016/S0093-6413(02)00252-5) (2002).
32. Dafalias, Y. & Taiebat, M. Anatomy of rotational hardening in clay plasticity. *Geotechnique* **63**, 1406–1418. <https://doi.org/10.1680/geot.12.P197> (2013).
33. Hashiguchi, K. & Chen, Z. P. Elastoplastic constitutive equation of soils with the subloading surface and the rotational hardening. *Int. J. Numer. Anal. Meth. Geomech.* **22**, 197–227. [https://doi.org/10.1002/\(SICI\)1096-9853\(199803\)22:3<197::AID-NAG914%3e3.0.CO;2-T](https://doi.org/10.1002/(SICI)1096-9853(199803)22:3<197::AID-NAG914%3e3.0.CO;2-T) (1998).
34. Yamakawa, Y. et al. Anisotropic subloading surface Cam-clay plasticity model with rotational hardening: Deformation gradient-based formulation for finite strain. *Int. J. Numer. Anal. Meth. Geomech.* **45**, 2321–2370. <https://doi.org/10.1002/nag.3268> (2021).
35. Hashiguchi, K., Mase, T. & Yamakawa, Y. Elaborated subloading surface model for accurate description of cyclic mobility in granular materials. *Acta Geotech.* **17**, 699–719. <https://doi.org/10.1007/s11440-021-01203-y> (2022).
36. Dafalias, Y. F., Manzari, M. T. & Papadimitriou, A. G. SANICLAY: Simple anisotropic clay plasticity model. *Int. J. Numer. Anal. Meth. Geomech.* **30**, 1231–1257 (2006).
37. Yao, Y., Gao, Z., Zhao, J. & Wan, Z. Modified UH model: Constitutive modeling of overconsolidated clays based on a parabolic Hvorslev envelope. *J. Geotech. Geoenviron. Eng.* **138**, 860–868. [https://doi.org/10.1061/\(ASCE\)GT.1943-5606.0000649](https://doi.org/10.1061/(ASCE)GT.1943-5606.0000649) (2012).
38. Tian, Y. & Yao, Y. P. Constitutive modeling of principal stress rotation by considering inherent and induced anisotropy of soils. *Acta Geotech.* **13**, 1299–1311. <https://doi.org/10.1007/s11440-018-0680-3> (2018).
39. Wang, Z., Yang, Y., Li, Y., Liu, S. & Zhou, P. Numerical simulation of cyclic shear tests considering the fabric change and principal stress rotation effects. *Int. J. Numer. Anal. Meth. Geomech.* **46**, 1409–1432. <https://doi.org/10.1002/nag.3351> (2022).
40. Gao, Z., Zhao, J., Li, X. S. & Dafalias, Y. F. A critical state sand plasticity model accounting for fabric evolution. *Int. J. Numer. Anal. Meth. Geomech.* **38**, 370–390. <https://doi.org/10.1007/s11440-018-0735-5> (2014).
41. Anandarajah, A. *Computational Methods in Elasticity and Plasticity. Solids and porous media* (Springer, 2010).
42. Tamagnini, R. An extended cam-clay model for unsaturated soils with hydraulic hysteresis. *Geotechnique* **54**, 223–228. <https://doi.org/10.1680/geot.2004.54.3.223> (2004).
43. Houlsby, G. The use of a variable shear modulus in elastic-plastic models for clays. *Comput. Geotech.* **1**, 3–13. [https://doi.org/10.1016/0266-352X\(85\)90012-6](https://doi.org/10.1016/0266-352X(85)90012-6) (1985).
44. Houlsby, G., Amorosi, A. & Rojas, E. Elastic moduli of soils dependent on pressure: a hyperelastic formulation. *Geotechnique* **55**, 383–392. <https://doi.org/10.1680/geot.2005.55.5.383> (2005).
45. Hashiguchi, K. Hypo-elastic and hyper-elastic equations of soils. *Int. J. Numer. Anal. Meth. Geomech.* **42**, 1554–1564. <https://doi.org/10.1002/nag.2804> (2018).
46. Houlsby, G., Amorosi, A. & Rollo, F. Non-linear anisotropic hyperelasticity for granular materials. *Comput. Geotech.* **115**, 103167. <https://doi.org/10.1016/j.compgeo.2019.103167> (2019).
47. Amorosi, A., Rollo, F. & Houlsby, G. T. A nonlinear anisotropic hyperelastic formulation for granular materials: Comparison with existing models and validation. *Acta Geotech.* **15**, 179–196. <https://doi.org/10.1007/s11440-019-00827-5> (2020).
48. Yamakawa, Y. Hyperelastic constitutive models for geomaterials: Extension of existing models to include finite strains and their comparison. *Comput. Geotech.* **143**, 104600. <https://doi.org/10.1016/j.compgeo.2021.104600> (2022).
49. McDowell, G. & Hau, K. A simple non-associated three surface kinematic hardening model. *Geotechnique* **53**, 433–437. <https://doi.org/10.1680/geot.2003.53.4.433> (2003).
50. Rowe, P. W. The stress-dilatancy relation for static equilibrium of an assembly of particles in contact. *Proc. R. Soc. Lond. Ser. A Math. Phys. Sci.* **269**, 500–527. <https://doi.org/10.1098/rspa.1962.0193> (1962).

51. Simo, J. & Taylor, R. A return mapping algorithm for plane stress elastoplasticity. *Int. J. Numer. Meth. Eng.* **22**, 649–670. <https://doi.org/10.1002/nme.1620220310> (1986).
52. Borja, R. I. Cam-clay plasticity, part II: Implicit integration of constitutive equation based on a nonlinear elastic stress predictor. *Comput. Methods Appl. Mech. Eng.* **88**, 225–240. [https://doi.org/10.1016/0045-7825\(91\)90256-6](https://doi.org/10.1016/0045-7825(91)90256-6) (1991).
53. Yang, Y., Yu, H.-S. & Kong, L. Implicit and explicit procedures for the yield vertex non-coaxial theory. *Comput. Geotech.* **38**, 751–755. <https://doi.org/10.1016/j.compgeo.2011.03.008> (2011).
54. Yamakawa, Y., Hashiguchi, K. & Ikeda, K. Implicit stress-update algorithm for isotropic cam-clay model based on the subloading surface concept at finite strains. *Int. J. Plast.* **26**, 634–658. <https://doi.org/10.1016/j.ijplas.2009.09.007> (2010).
55. Sloan, S. W. Substepping schemes for the numerical integration of elastoplastic stress–strain relations. *Int. J. Numer. Meth. Eng.* **24**, 893–911. <https://doi.org/10.1002/nme.1620240505> (1987).
56. Sloan, S. W., Abbo, A. J. & Sheng, D. Refined explicit integration of elastoplastic models with automatic error control. *Eng. Comput.* **18**, 121–194. <https://doi.org/10.1108/02644400110365842> (2001).
57. Sun, Z. C., Chu, J. & Xiao, Y. Formulation and implementation of an elastoplastic constitutive model for sand-fines mixtures. *Int. J. Numer. Anal. Meth. Geomech.* **45**, 2682–2708. <https://doi.org/10.1002/nag.3282> (2021).
58. Hu, C. & Liu, H. Implicit and explicit integration schemes in the anisotropic bounding surface plasticity model for cyclic behaviours of saturated clay. *Comput. Geotech.* **55**, 27–41. <https://doi.org/10.1016/j.compgeo.2013.07.012> (2014).
59. Navarro, V., Candel, M., Barenca, A., Yustres, A. & Garcia, B. Optimisation procedure for choosing cam clay parameters. *Comput. Geotech.* **34**, 524–531. <https://doi.org/10.1016/j.compgeo.2007.01.007> (2007).
60. Pestana, J. M., Whittle, A. J. & Gens, A. Evaluation of a constitutive model for clays and sands: Part II—clay behaviour. *Int. J. Numer. Anal. Meth. Geomech.* **26**, 1123–1146. <https://doi.org/10.1002/nag.238> (2002).
61. Zhang, F., Ye, B. & Ye, G. Unified description of sand behavior. *Front. Arch. Civ. Eng. China* **5**, 121–150. <https://doi.org/10.1007/s11709-011-0104-z> (2011).
62. Hu, X. R., Dong, X. L., Chen, X. Y. & Hu, B. Y. The elasto-plastic constitutive model and tri-axial numerical simulation for saturated over-consolidated clay. *Chin. J. Appl. Mech.* **35**, 28–35. <https://doi.org/10.11776/cjam.35.01.B115> (2018).
63. Verdugo, R. & Ishihara, K. The steady state of sandy soils. *Soils Found.* **36**, 81–91. https://doi.org/10.3208/sandf.36.2_81 (1996).
64. Nakai, K. *An Elasto-Plastic Constitutive Modeling of Soils Based on the Evolution Laws Describing Collapse of Soil Skeleton Structure, Loss of Overconsolidation and Development of Anisotropy* (Nagoya University, 2005).

Acknowledgements

The authors would like to acknowledge the financial support from the National Natural Science Foundation of China (Grant No.42177128, 42077236, 42011530170), and sponsored by Sichuan Science and Technology Program (Grant No. 2021YFH0037, 2021YFH0320, 2019JDJQ0018).

Author contributions

X.W. proposed the theoretical model, compiled the code and wrote the original manuscript. R.Y. analyzed the data, plotted the figures and helped with editing manuscript text. K.C. validated the simulation results, as well as improved the manuscript presentation. All authors reviewed the manuscript.

Competing interests

The authors declare no competing interests.

Additional information

Correspondence and requests for materials should be addressed to K.C.

Reprints and permissions information is available at www.nature.com/reprints.

Publisher's note Springer Nature remains neutral with regard to jurisdictional claims in published maps and institutional affiliations.



Open Access This article is licensed under a Creative Commons Attribution 4.0 International License, which permits use, sharing, adaptation, distribution and reproduction in any medium or format, as long as you give appropriate credit to the original author(s) and the source, provide a link to the Creative Commons licence, and indicate if changes were made. The images or other third party material in this article are included in the article's Creative Commons licence, unless indicated otherwise in a credit line to the material. If material is not included in the article's Creative Commons licence and your intended use is not permitted by statutory regulation or exceeds the permitted use, you will need to obtain permission directly from the copyright holder. To view a copy of this licence, visit <http://creativecommons.org/licenses/by/4.0/>.

© The Author(s) 2022